Supplementary Information

Synergism induced exceptional capacity and complete reversibility in Mg-Y thin films: enabling next generation metal hydride electrodes

Kai Fu[1,2], Jun Chen[1], Rui Xiao[1], Jie Zheng[1], Wenhuai Tian[2]* and Xingguo Li[1]*

[1]Beijing National Laboratory of Molecular Sciences, State Key Laboratory of Rare Earth Materials Chemistry and Applications, College of Chemistry and Molecular Engineering, Peking University, Beijing 100871, China

[2] Department of Materials Physics and Chemistry, University of Science and Technology Beijing, NO. 30, Xueyuan Road, Beijing 100083, China

E-mail addresses: xgli@pku.edu.cn (X. Li), wenhuaitian@ustb.edu.cn (W. Tian).

1 The derivation of equation (5) in the main text: Relationship between E_{eq} and ΔG_{deH}^{o}

It has long been recognized that there is a direct relationship between the equilibrium potential of a metal hydride electrode (E_{eq}), i.e. the discharge plateau in the potential profile attributed to reaction (1), and the Gibbs energy change of the relevant dehydrogenation reaction (ΔG_{deH}^{o} of reaction (2))

$$MH\ (s) - e^{-} + OH^{-} \rightarrow M\ (s) + H_2O\ (l) \quad (1)$$

$$MH\ (s) \rightarrow M\ (s) + 1/2\ H_2\ (g) \quad (2)$$

This relationship can be expressed by equation (3). The derivation can be found in Ref. [1, 2].

$$E_{eq} = \Delta G_{deH}^{o}/nF\ vs.\ RHE \quad (3)$$

Here *n* is the number of electrons involved in the discharging reaction and *F* the Faraday constant.

When using eV as the unit for energy, the left side of equation (3) numerically equals the Gibbs free energy change of the dehydrogenation reaction (expressed in eV). Thus the equilibrium potential of a metal hydride electrode (E_{eq} (vs. RHE) of reaction (1)) numerically equals the Gibbs free energy change of the relevant dehydrogenation reaction (ΔG_{deH}^{o} (eV) of reaction (2)), which can be expressed by equation (4).

$$E_{eq}\ (vs.\ RHE) = \Delta G_{deH}^{o}\ (eV) \quad (4)$$

For convenience, we use eV as the unit for energy in this work unless otherwise indicated. All the measured potential (φ^{o}) versus the Hg/HgO reference electrode are converted into values versus the reversible hydrogen electrode (RHE) through the relationship of:

$$\varphi^{o}\ (\text{vs. RHE}) = \varphi^{o}\ (\text{vs. Hg/HgO}) + 0.0977\ V + 0.05916 \times pH \quad (5)$$

2 The schematic energy diagram of two potential pathways

The formation of intermetallic can be used for tailoring Gibbs free energy and inducing synergetic effect in dehydrogenation process, which is critically necessary for breaking through the thermodynamic/kinetic barriers and achieving complete reversibility in the absence of non-hydrogen-absorbing elements (B). Fig. S1 demonstrates the above design strategy using an energy diagram. The thermodynamic data (ΔG^{o}_{deH}) for the relevant chemical reactions are shown in Table S1.

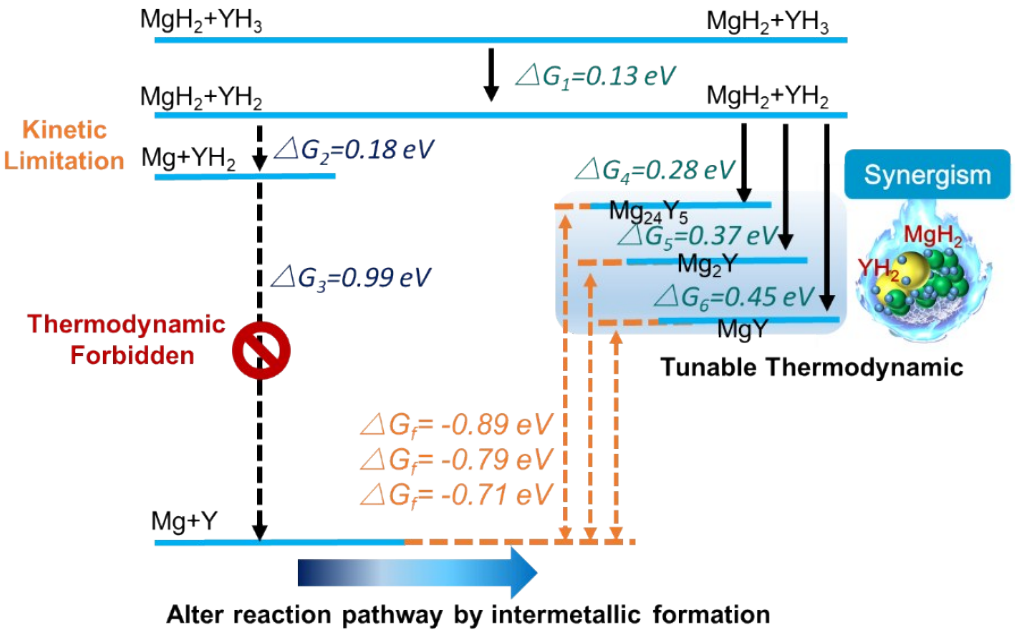

Fig. S1 The schematic energy diagram of two potential pathways.

Table S1

Thermodynamic data for the relevant dehydrogenation reactions at room temperature (25 °C).

Reaction	$\triangle G_{deH}$ (kJ mol^{-1}H$_2$)	$\triangle G$ (eV)	Reference
$YH_3 \rightarrow YH_2 + H_2(g)$	13.0	0.13	3
$MgH_2 \rightarrow Mg + H_2(g)$	34.2	0.18	4
$YH_2 \rightarrow Y + H_2(g)$	190.3	0.99	5
$MgH_2 + YH_2 \rightarrow Mg_{24}Y_5 + H_2(g)$	53.4	0.28	4, 5, 6
$MgH_2 + YH_2 \rightarrow Mg_2Y + H_2(g)$	68.4	0.37	4, 5, 6

$MgH_2 + YH_2 \rightarrow MgY + H_2(g)$	86.2	0.45	4, 5, 6

The equilibrium potential for the phase transformation during discharging can be directly obtained from the Gibbs free energy change of the relevant dehydrogenation reaction using equation (4), as shown in Table S2.

Table S2

Equilibrium potential for the phase transformation together with Gibbs free energy change of the relevant dehydrogenation reaction.

Reaction	$E_{eq}\,(V\ vs.\ RHE) = \Delta G^{o}_{deH}\,(eV)$
$YH_3 - e^- + OH^- \rightarrow YH_2 + H_2O$	0.13
$MgH_2 - e^- + OH^- \rightarrow Mg + H_2O$	0.18
$YH_2 - e^- + OH^- \rightarrow Y + H_2O$	0.99
$MgH_2 + YH_2 - e^- + OH^- \rightarrow Mg_{24}Y_5 + H_2O$	0.28
$MgH_2 + YH_2 - e^- + OH^- \rightarrow Mg_2Y + H_2O$	0.37
$MgH_2 + YH_2 - e^- + OH^- \rightarrow MgY + H_2O$	0.45

3 Contribution of the Pd cap layer

The surface Pd layer provides a H permeable layer for both efficient catalytic generation of surface adsorbed hydrogen and protection of the Mg-Y sample from oxidation. As can be seen from Fig. S2, the $Mg_{24}Y_5$ thin film sample without the Pd protection layer barely shows any capacity, emphasizing the unique role of the surface Pd layer.

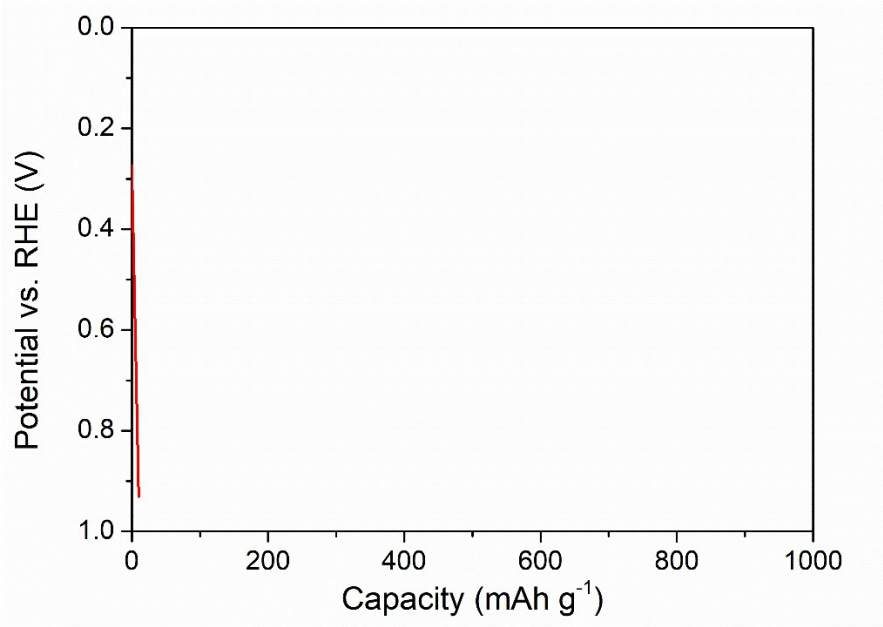

Fig. S2 Potential profiles of the $Mg_{24}Y_5$ thin film sample without the Pd protection layer.

Pd can absorb and desorb hydrogen at room temperature and does not pulverize after hydrogen insertion. The limit of absorption of nanometer-sized Pd at normal pressures is only $PdH_{0.5}$ (equivalent to 0.47 wt.%.)[7, 8].In addition, the theoretical discharge plateau of reaction (6) is around -0.12 V vs. RHE (See Table S3). No discharge plateau can be observed in this region. Thus the hydrogen storage capacity of the 10 nm Pd cap layer can be neglected.

$$PdH - e^- + OH^- \rightarrow Pd + H_2O \quad (6)$$

Table S3. Thermodynamic data for the reaction (6)

Reaction	$\Delta G^o_{deH}\,(eV) = \varphi^o$ (V vs. RHE)
$PdH - e^- + OH^- \rightarrow Pd + H_2O$	-0.12 [9]

The cyclic voltammetry (CV) curves of the $Mg_{24}Y_5$/Pd thin film on the activation procedure are shown in Fig. S3. The pronounced cathodic wave around 0.65 V vs. RHE was assignable to the electroreduction of PdO to Pd[10-12].

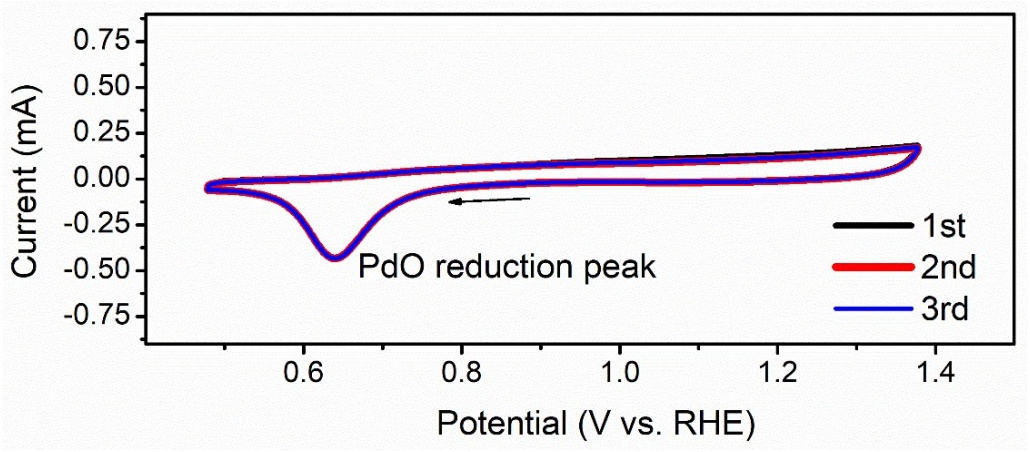

Fig. S3 Cyclic voltammogram curves of the $Mg_{24}Y_5$/Pd thin film on the activation procedure.

4 Repeatability of the results

Both the mass loadings and the discharge capacities of $Mg_{24}Y_5$ and Mg_2Y films have been repeatedly verified.

The mass loading of a sample is determined by averaging five measurements. The standard deviations of the mass loadings when measuring the same samples are given in Fig. S4.

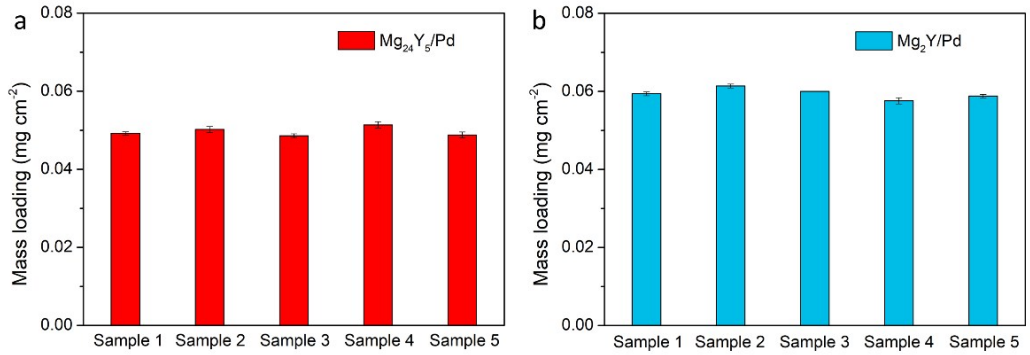

Fig. S4 The standard deviations of the mass loadings when measuring the same sample.

The discharge capacities of different samples were obtained based on the discharge curves and the mass of active materials. To ensure the reliability, the discharge capacities of $Mg_{24}Y_5$/Pd and Mg_2Y/Pd films were repeatedly verified and determined by using the average values of five samples (see Fig. 2a in the main text).

5 Structural characterization of the virgin films

The XRD patterns of all the pristine Mg-Y/Pd thin films with different Mg-Y ratio are shown in Fig. S5. All the samples show a strong preferred orientation, which is

characteristic for thin films. The (111) peak of Pd (ICSD No. 648674) is observed in all the samples. For pure Mg and pure Y thin films, Mg (002) peak and Y (002) peak can be observed around 31.2° (ICSD No. 52260) and 34.6° (ICSD No. 653450) respectively. Addition of 10 at.% Y to Mg film causes lower shift of the Mg (002) peak, which is attributed to the lattice expansion due to Y substitution. While in the other composition, Mg and Y atoms in the vapor phase can react directly during the deposition process to form stable Mg-Y binary intermetallic. For $Mg_{0.83}Y_{0.17}$/Pd, $Mg_{0.66}Y_{0.34}$/Pd and $Mg_{0.50}Y_{0.50}$/Pd samples, only $Mg_{24}Y_5$, Mg_2Y and MgY intermetallic can be observed respectively. The other pristine thin films were composed of multi-phases, which is in accordance with the Mg-Y binary phase diagram.

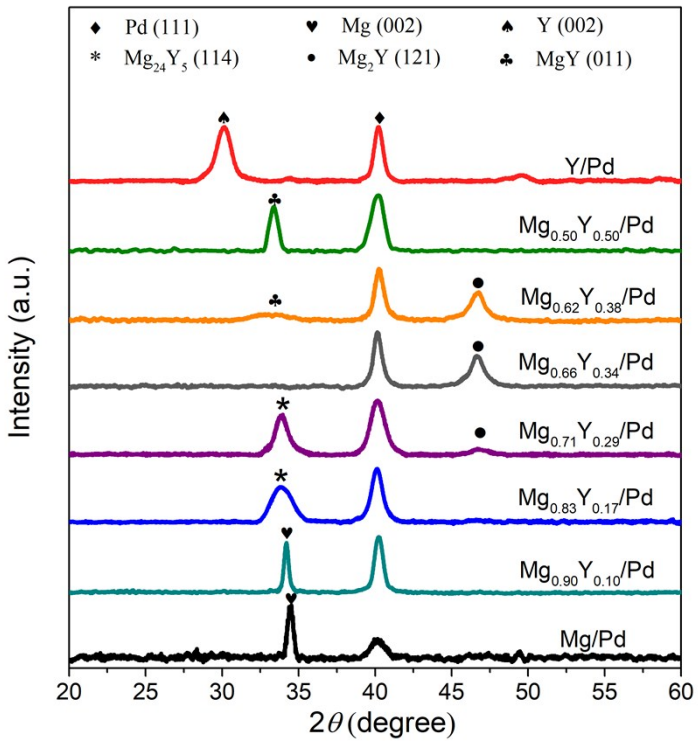

Fig. S5 XRD patterns of pristine Mg-Y/Pd films with various Mg-Y ratio.

The XRD patterns of the pristine Mg/Pd, $Mg_{0.82}Y_{0.18}$/Pd and Y/Pd films are shown in Fig. S6a. The (111) peak of Pd (ICSD No. 648674) is observed in all the samples. An intense peak around 34.1° indicates that the pure Mg (ICSD No. 52260) film preferentially grow along the (002) direction. The Y/Pd thin film exhibits a single strong (002) peak of hexagonal Y (ICSD No. 653450). For the $Mg_{0.82}Y_{0.18}$/Pd thin film,

we find only $Mg_{24}Y_5$ peaks, in accordance with the Mg-Y phase diagram. Mg and Y atoms in the vapor phase can react directly during the deposition process to form stable $Mg_{24}Y_5$ intermetallic.

The surface morphologies of the Mg/Pd, $Mg_{24}Y_5$/Pd and Y/Pd films are shown in Fig. S6b-d. The Mg/Pd film is composed of hexagonal particles with uniform particle size approximately 100 nm. The Y/Pd film is composed of irregular nanoparticles with grain size around 20 nm. For the $Mg_{24}Y_5$/Pd film, the grain size is only approximately 10 nm, smaller than that of both Mg/Pd and Y/Pd films.

The HRTEM and corresponding SAED patterns are shown in Fig. S6e-g. Lattice fringes corresponding to Mg, $Mg_{24}Y_5$ and Y can be observed in the corresponding samples, together with that from the Pd capping layer. The SAED patterns exhibit more diffraction features compared to the XRD pattern, which further confirms the phase structure of each film.

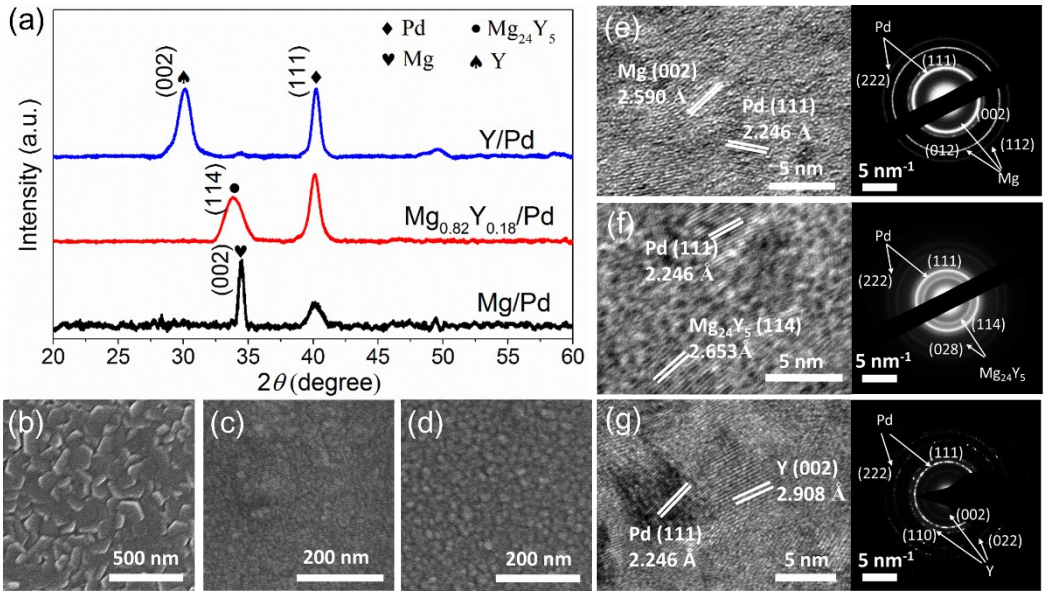

Fig. S6 Structural characterization of the virgin films. (a) XRD patterns of Mg/Pd, $Mg_{24}Y_5$/Pd and Y/Pd films. (b-d) SEM images of Mg/Pd (b) $Mg_{24}Y_5$/Pd (c) and Y/Pd (d) films. e-g, High-resolution TEM images and corresponding SAED patterns of Mg/Pd (e), $Mg_{24}Y_5$/Pd (f) and Y/Pd (g) films.

5 Area capacities of various films

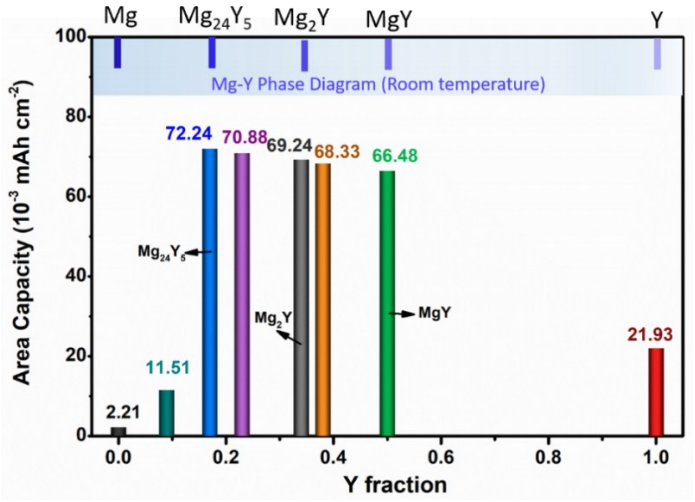

Fig. S7 Area capacities of various films.

6 The cyclic stabilities of the $Mg_{24}Y_5$/Pd film

The cyclic stability of the $Mg_{24}Y_5$/Pd film during galvanostatic charge/discharge processes is shown in Supplementary Fig. S8. No activation process was required for the film before reaching the largest discharge capacities, which is very favorable for practical application of electrochemical hydrogen storage. The maximum capacity was at near theoretical and achieved to ~1523 mAh g^{-1} at first cycle and ~92% of which (~1397 mAh g^{-1}) could be maintained after 20 cycles (Fig. S7). The capacity is slightly decreased after that and capacity retention rate of 82% is maintained after 50 cycles (~1246 mAh g^{-1}). As can be seen from Fig. S9, the capacity degradation of the electrodes is attributed to the shortening of the second discharge plateau around 0.30 V.

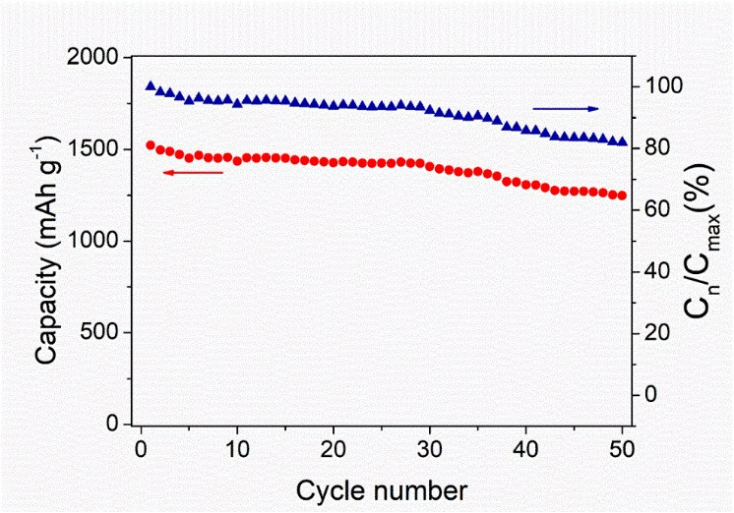

Fig. S8 Discharge capacities and the corresponding capacity retention rates of $Mg_{24}Y_5$/Pd films within 50 cycles.

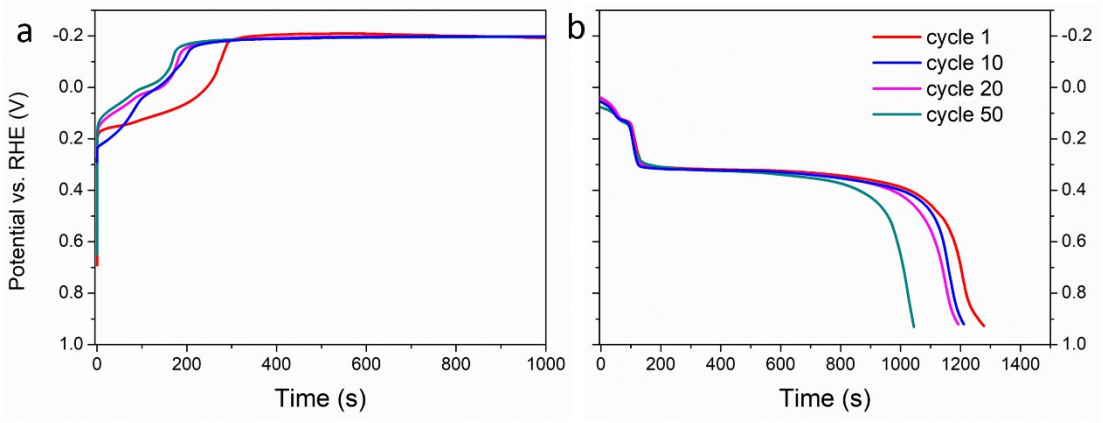

Fig. S9 Selected potential profiles during galvanostatic charge/discharge cycles.

7 The galvanostatic intermittent titration technique (GITT) measurement

To clarify the overpotential, the galvanostatic intermittent titration technique (GITT) has been performed on the $Mg_{24}Y_5$ film (see Fig. S10). The MH electrode was charged with a constant current of 1 mA cm^{-2} for 50 s followed by a current off relaxation period of 1000 s. During discharging the measurement was performed with a current of 0.2 mA cm^{-2} for 50 s followed by a resting period of 1000s. The obtained equilibrium curve (open symbols) in the charge and discharge process are drew with green and blue lines respectively. The insets shows the potential response and subsequent relaxation period of typical GITT pulses at the plateau (indicated by the arrow) and shows that after the current interruption the potential quickly stabilizes to the new equilibrium potential.

In the case of electrochemical charging, a parasitic reaction, known as the hydrogen evolution reaction (HER), can occur according to reaction (7).

$$H_2O + e^- \rightarrow 1/2H_2 + OH^- \quad (7)$$

Note that at the end of the charge process, i.e. the second plateau region in the charge profile, reaction (7) is thermodynamic favorable and competes with the hydride-formation reaction. This reaction exhibits large overpotential in the absence of HER catalyst. Thus electrochemically obtained isothermal curves for discussing thermodynamics of MH electrode are generally determined during discharging as incorrect calculations of the equilibrium potential and hydrogen content caused by the parasitic HER are then avoided.

It is clear that the overpotential remains nearly constant (generally < 0.02 V) throughout the entire discharge process, only to increase significantly at the very end of the discharge process. This latter behavior is expected as the thin film reaches its hydrogendepleted state. The inset shows the potential response and subsequent relaxation period of typical GITT pulse at the second discharge plateau (indicated by the arrow) and shows that after the current interruption the potential quickly stabilizes to the new equilibrium potential.

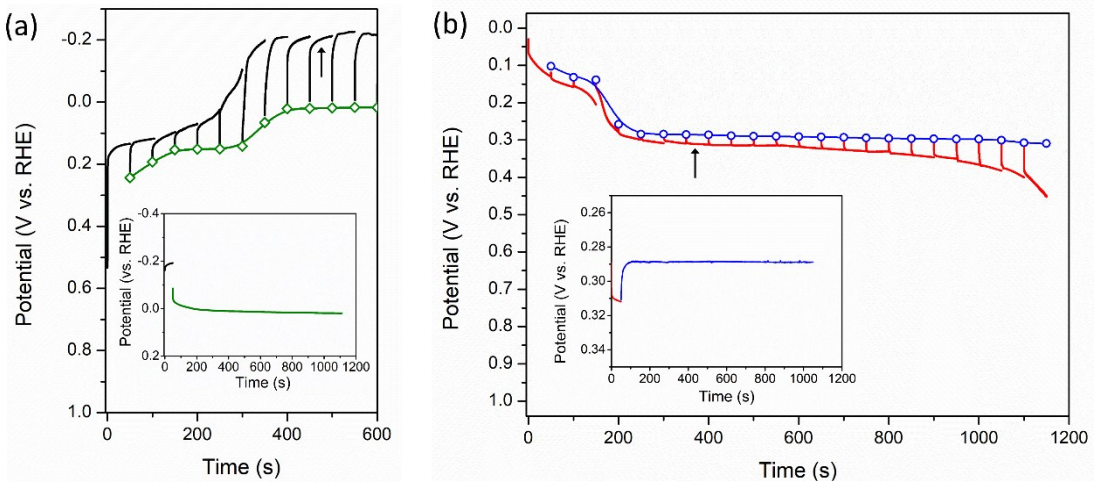

Fig. S10 GITT curves of $Mg_{24}Y_5$/Pd film as a function of time. (a) GITT curves in the initial charge process. (b) GITT curves in the discharge process. The insets show the potential response and subsequent relaxation of a particular GITT pulse at the hydrogen evolution reaction plateau and at the second discharge plateau (indicated by the arrows).

8 Substrates

As noted in the manuscript, the unique optical switching property of thin film electrodes enables in situ monitoring the hydrogen content in the film during electrochemical processes. So we use transparent glass substrate in this work to carry out synchronized electrochemical and optical transmittance measurements.

The glass substrate is not an electronic conductor, but the Pd capped thin film is electronically conductive. Prior to measurements, the internal resistant of the cell has been measured and was about 0.7 Ω. The current collector (substrate) needs to be an electronic conductor in real batteries. To be prudent, $Mg_{24}Y_5$/Pd thin film were also deposited onto titanium (Ti) substrate, which is an electronically conductive substrate. The potential profiles of $Mg_{24}Y_5$/Pd thin film deposited on Ti and glass substrates during first galvanostatic charge/discharge cycle are compared and are shown in Fig. S11. Similar results were found in these two samples.

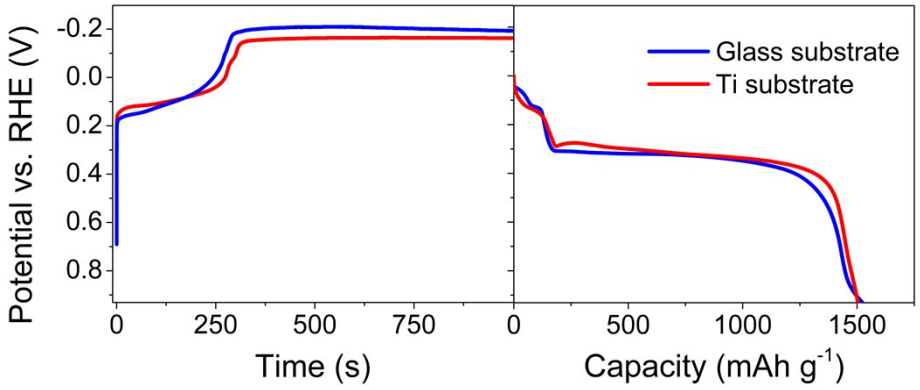

Fig. S11 Comparison of potential profiles of $Mg_{24}Y_5$/Pd thin film deposited on Ti and glass substrates during first galvanostatic charge/discharge cycles.

9 Kinetics

According to the hydrogen energy diagram, reversible H storage in Mg is not limited by thermodynamics. However, the 250 nm Mg/Pd film is extremely inactive for electrochemical hydrogen storage, which can only be explained by the poor kinetics. The hydrogen diffusion coefficients (D_H) in the film is a critical kinetic parameter, which can be determined by fitting the time dependent current profile in a potential

transient using the Hagi's model . When time t is long ($>3L^2/\pi^2 D_H$), the current density J_H could be described as: $\ln(J_H) = -\pi^2 D_H/4d^2 t$ + constant , where d is the thickness of the film. As shown in Fig. S12, the obtained D_H for the Mg/Pd film is only 4.2×10^{-15} cm^2 s^{-1}. The slow H diffusion is the major reason for the poor hydrogen storage performance of the Mg/Pd thin film. In order to achieve full hydrogenation of Mg, the domain size of Mg should be kept small. Our previous study shows that full hydrogenation of Mg/Pd film thicker than 100 nm is difficult in both gas phase and electrochemical process.

Compared to Mg, H diffusion in Y hydride is three orders of magnitude faster (D_H $=9.05 \times 10^{-12}$ cm^2 s^{-1}). According to the XRD results, hydrogenation of $Mg_{24}Y_5$ leads to phase segregation. The first step is formation of small domains of Mg and Y hydride. The Y hydride provides a fast H diffusion path, which is critical to achieve full hydrogenation of Mg. The effective enhancement of H diffusion by including Y hydride can be inferred by the high D_H of the Mg_2Y/Pd sample, which is measured to be 2.37×10^{-13} cm^2 s^{-1} and two orders of magnitude faster than pure Mg/Pd sample. During the dehydrogenation process, the ΔG^{o}_{deH} for MgH_2 is about 0.2 eV more negative than that of synergistic dehydrogenation of MgH_2 and YH_2. However, the kinetic limitation significantly inhibit the separate decomposition of MgH_2 in vicinity to the YH_2 domains. The synergistic dehydrogenation can overcome this kinetic limitation, leading to a desorption of all the rest H in one single step.

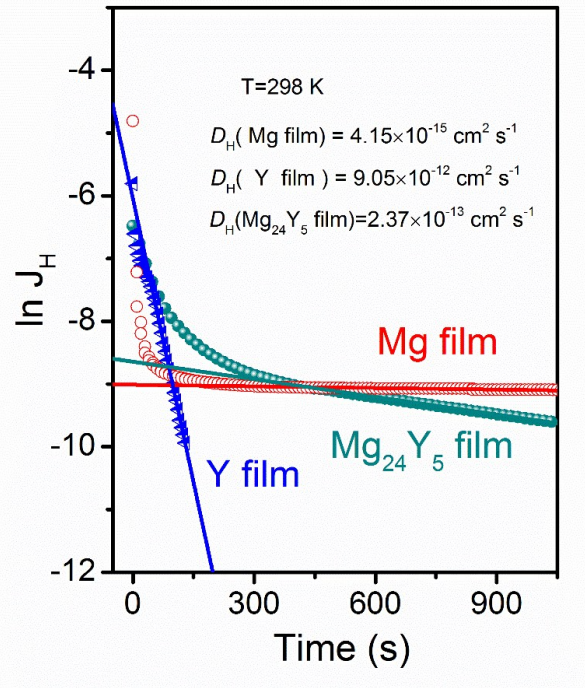

Fig. S12 The hydrogen diffusion coefficients of Mg/Pd, Y/Pd and $Mg_{24}Y_5$/Pd films at room temperature. The straight lines is the linear fit according to the data.

9 Theoretical energy densities of different electrochemical couples

The capacities of anode and cathode active materials are summarized in Supplementary Table S3.

Table S3. Capacities of anode and cathode active materials

Practical application			
Anode	Capacity (mAh g^{-1})	Cathode	Capacity (mAh g^{-1})
$LaNi_5$	372	β-$Ni(OH)_2$	289
La_3MgNi_{14} (A_2B_7)	410	β-$Ni(OH)_2$	289
La_2MgNi_9 (AB_3)	418	β-$Ni(OH)_2$	289
$Mg_{24}Y_5$	1642	β-$Ni(OH)_2$	289
Further development			
Anode	Capacity (mAh g^{-1})	Cathode	Capacity (mAh g^{-1})
$LaNi_5$	372	O_2	3350
$Mg_{24}Y_5$	1642	O_2	3350

We further assemble full Ni-$Mg_{24}Y_5H$ batteries by pairing the $Mg_{24}Y_5$ film anode

and $Ni(OH)_2$ cathode. The area of each MH film electrode is 2 cm^2. As demonstrations, two Ni-$Mg_{24}Y_5H$ batteries were connected in series to double the output voltage and power a light-emitting-diode (LED) watch (1.5 V, 3μA) for a long time (The inset digital image of Fig. S13). Voltage profiles of the two tandem Ni-$Mg_{24}Y_5H$ batteries during discharging are shown in Fig. S13. The batteries ensures a voltage output higher than 1.5 V for more than 10 h with a constant current of 3 μA (~1.5 μA cm^{-2} for $Mg_{24}Y_5$ film, the rated current of the LED watch).

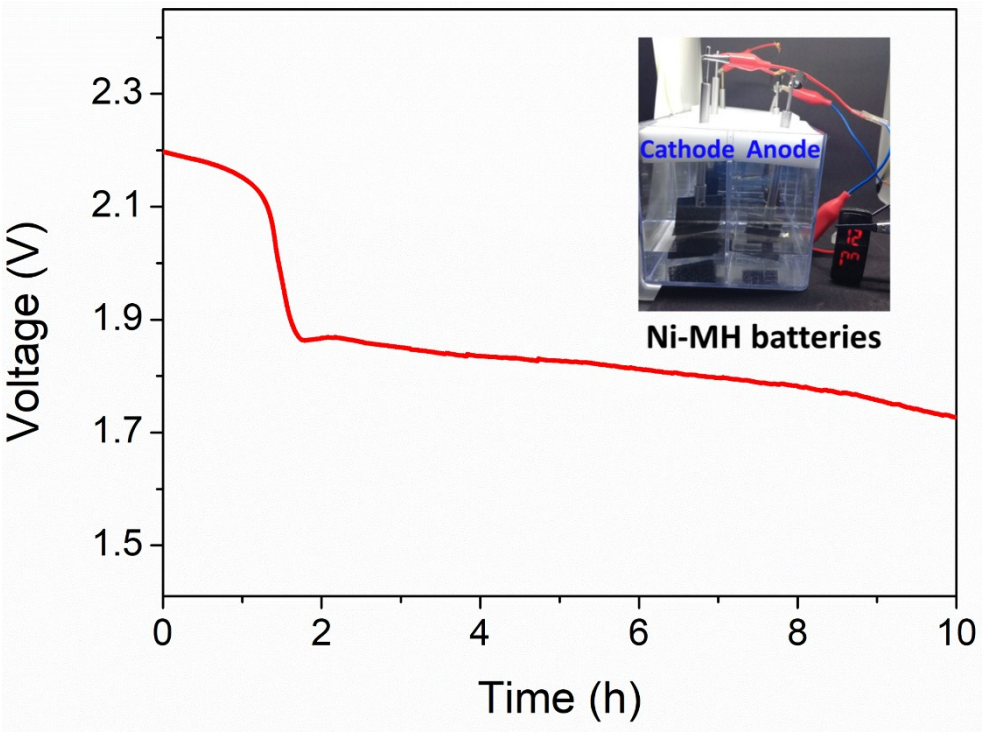

Fig. S13. Voltage profiles of the two tandem full Ni-$Mg_{24}Y_5H$ batteries; The inset digital image shows the light-emitting diode watch lit by the Ni-$Mg_{24}Y_5H$ batteries.

1. J. J. G. Willems, Philips J. Res. Suppl. 1984, **39**, 1 –94.
2 .P. H. L. Notten, in *Interstitial Intermetallic Alloys*, eds. F. Grandjean, G. J. Long and K. H. J. Buschow, Springer Netherlands, Dordrecht, 1995, DOI: 10.1007/978-94-011-0295-7_7, pp. 151-195.
3. R. Griessen, J. N. Huiberts, M. Kremers, A. T. M. vanGogh, N. J. Koeman, J. P. Dekker and P. H. L. Notten, *J. Alloys Compd.*, 1997, **253**, 44-50.
4. H. Y. Shao, G. B. Xin, J. Zheng, X. G. Li and E. Akiba, *Nano Energy*, 2012, **1**, 590-601.
5 .C. E. Lundin and J. P. Blackledge, *J Electrochem Soc*, 1962, **109**, 838-842.
6. O. B. Fabrichnaya, H. L. Lukas, G. Effenberg and F. Aldinger, *Intermetallics*, 2003, **11**, 1183-1188.

7 .T. Ishimoto and M. Koyama, *J. Chem. Phys.*, 2018, **148**, 5.
8. G. Q. Li, H. Kobayashi, J. M. Taylor, R. Ikeda, Y. Kubota, K. Kato, M. Takata, T. Yamamoto, S. Toh, S. Matsumura and H. Kitagawa, *Nat. Mater.*, 2014, **13**, 802-806.
9. J. M. Joubert and S. Thiébaut, *J. Nucl. Mater.*, 2009, **395**, 79-88.
10. W. C. Sheng, M. Myint, J. G. G. Chen and Y. S. Yan, *Energy Environ. Sci.*, 2013, **6**, 1509-1512.
11. W. J. Huang, X. Y. Ma, H. Wang, R. F. Feng, J. G. Zhou, P. N. Duchesne, P. Zhang, F. J. Chen, N. Han, F. P. Zhao, J. H. Zhou, W. B. Cai and Y. G. Li, *Adv. Mater.*, 2017, **29**, 8.
12. H. B. Liao, C. Wei, J. X. Wang, A. Fisher, T. Sritharan, Z. X. Feng and Z. C. J. Xu, *Adv. Energy Mater.*, 2017, **7**, 7.